Local seismicity around the Chain Transform Fault at the Mid-Atlantic Ridge from OBS observations

David Schlaphorst[1,2]*, Catherine A. Rychert[3], Nicholas Harmon[3], Stephen P. Hicks[4], Petros Bogiatzis[3], J-Michael Kendall[5], Rachel E. Abercrombie[6]

(*corresponding author: dschlaphorst@fc.ul.pt)

[1] Instituto Dom Luiz (IDL), Faculdade de Ciências, Universidade de Lisboa, Campo Grande, 1749-016 Lisboa, Portugal.

[2] School of Earth Sciences, University of Bristol, Wills Memorial Building, Queens Road, Bristol BS8 1RJ, UK.

[3] Ocean and Earth Science, University of Southampton, National Oceanography Centre, Southampton, UK

[4] Department of Earth Science and Engineering, Imperial College London, UK.

[5] Department of Earth Sciences, University of Oxford, UK.

[6] Department of Earth & Environment, Boston University, USA.

Summary

Seismicity along transform faults provides important constraints for our understanding of the factors that control earthquake ruptures. Oceanic transform faults are particularly useful due to their relatively simple structure in comparison to continental counterparts. The seismicity of several fast-moving transform faults has been investigated by local networks, but as of today there have not been many studies of slower spreading centres. Here we present the first local seismicity catalogue based on event data recorded by a temporary broadband network of 39 ocean bottom seismometers located around the slow-moving Chain Transform Fault (CTF) along the Mid-Atlantic Ridge (MAR) from March 2016 to March 2017. Locations are constrained by simultaneously inverting for a 1-D velocity model informed by the event P- and S-arrival times. Depths and focal mechanisms of the larger events are refined using deviatoric moment tensor inversion. We find a total of 972 events in the area. Most of the seismicity is located at the CTF (700) and Romanche transform fault (94) and the MAR (155); a smaller number (23) can be observed on the continuing fracture zones or in intraplate locations. The ridge events are characterised by normal faulting and most of the transform events are characterised by strike slip faulting, but with several reverse mechanisms that are likely related to transpressional stresses in the region. CTF events range in magnitude from 1.1 to 5.6 with a magnitude of completeness around 2.3. Along the CTF we calculate a *b*-value of 0.81 ± 0.09. The event depths are mostly shallower than 15 km below sea level (523), but a small number of high-quality earthquakes (16) are located deeper, with some (8) located deeper than the brittle-ductile transition as predicted by the 600˚C-isotherm from a simple thermal model. The deeper events could be explained by the control of seawater infiltration on the brittle failure limit.

Introduction

The factors that dictate the location, size and style of earthquake faulting are fundamental for our understanding of hazard and hazard mitigation (e.g., Slemmons et al., 1986). Oceanic transform faults (OTF), such as those that connect the many fragmented sections of the slow spreading Mid-Atlantic Ridge, are an ideal place to investigate the earthquake cycle. While not a great risk to humans themselves due to their often remote locations, OTFs are thought to be relatively simple in terms of thermal structure, fault zone geometry, slip rate and rheology in comparison to more hazardous continental counterparts such as the San Andreas fault. Therefore, the study of earthquakes around OTFs provides important constraints to inform hazard assessments in continental areas. Ocean lithosphere is characterised by relatively homogenous composition, with mafic to ultra-mafic lithologies. In addition, deformation tends to be localised in a narrow zone, roughly 20 to 30 km wide (Fox & Gallo 1984) with nearly vertically oriented faults on which total motions should roughly correspond to ridge spreading rates. Finally, the region of potential seismic slip is also well-predicted by the region shallower than the 600˚C isotherm predicted by simple thermal models such as the halfspace cooling model (e.g., Abercrombie & Ekström, 2001).

However, a vast majority of events cannot be detected around OTFs, due to their general inaccessibility. Being in the middle of the ocean, the closest landmasses and, thus, seismic land stations are often located at teleseismic distances. Previous studies have used teleseismic data to investigate earthquake sources along OTFs (e.g., Engeln et al., 1986; Bergman & Solomon, 1988; Abercrombie & Ekström, 2001). However, smaller events are not recorded teleseismically, and the magnitude of completeness offered by global monitoring networks is high. In particular, this affects the observation of microseismicity around the brittle-ductile

transition. Furthermore, the use of a non-local velocity model can influence the accuracy of hypocentre depth localisations.

Over the last decade the installation of dense ocean bottom seismometer (OBS) networks has enabled the more detailed study of local seismicity along Pacific OTFs, e.g., at the Discovery OTF (McGuirre et al., 2012) or the Blanco OTF (Kuna et al., 2019). However, spreading rates in the Pacific are mostly classified as intermediate or even fast (> 60 mm/yr), whereas the MAR is a slow-spreading ridge, which could have an effect on the local seismicity. The Chain and Romanche, as well as other OTFs in the North Atlantic are constructed of very thin, highly serpentinized crust (Detrick et al., 1993) and teleseismic earthquakes can be observed in the shallow mantle beneath (Abercrombie & Ekström, 2001). While there have been studies using OBS networks to investigate ridge segments or ridge-transform intersections in the Atlantic (e.g., Toomey at al., 1985; Grevemeyer et al., 2013, Gregory et al., 2021; Yu et al., 2021), local studies of Atlantic OTFs have been sparse.

From March 2016 to March 2017, a temporary network of 39 seismic ocean bottom seismometers (OBS) was deployed around the Chain transform fault (CTF) on the MAR and continuing eastward fracture zone (FZ) as part of the PI-LAB ("Passive Imaging of the Lithosphere-Asthenosphere Boundary") project and EURO-LAB (Experiment to Unearth the Rheological Oceanic Lithosphere-Astenosphere Boundary) (Fig. 1; Agius et al., 2018, 2021; Harmon et al., 2018, 2020, 2021; Hicks et al., 2020; Bogiatzis et al., 2020; Wang et al., 2020; Rychert et al., 2021; Saikia et al., 2020, 2021; Leptokaropoulos et al., 2021). The CTF zone has a length of 300 km and varies in thickness between 7 km and 20 km with an African Plate half-spreading rate of 18.2mm/yr and a South American Plate half spreading rate of 15.7mm/yr (Demets et al., 1994; Harmon et al., 2018). The aim of the experiment was to

cover an area of transition from oceanic crust formation at the MAR to older plate ages away from the ridge; the setup was chosen to facilitate the observation of thickening oceanic lithosphere relative to increasing plate age (Rychert et al., 2021). During the same time, the International Seismic Centre (ISC) recorded 40 earthquakes in the region, of which 23 are located in the vicinity of the Romanche transform fault (RTF), 7 close to the CTF and 8 around the MAR; 2 earthquakes were found on the inactive part of the Chain FZ.

In this study, we present the first catalogue of local seismicity around the equatorial MAR near the CTF, together with a 1D velocity model of the oceanic crust and upper mantle. The catalogue provides event times, hypocentre locations and magnitude information. We investigate small-scale seismicity variations along the CTF, the adjacent Chain FZ and the adjoining sections of the MAR. We also compute earthquake-magnitude distribution at CTF and RTF. Furthermore, we investigate the seismicity in relation to the depth of the brittle ductile region predicted by simple thermal models.

Method

Localisation

The data were recorded by the 39 PI-LAB OBS stations during their one-year deployment (Fig. 1, Table 1). The stations are mostly distributed in two lines north and south of the CTF and eastern FZ continuation with an average spacing of 40 km around the active part. On the CTF, the typical minimum station distance to the events is around 50 km. We use a Butterworth bandpass filter with corner frequencies of 4Hz and 18Hz, which enhances the signal-to-noise ratio in a marine environment using OBS instruments. The a priori temporary

118 set of picks is created using automated picks from a short-time average divided by long time
119 average (STA/LTA) detector. We use a 1D velocity model that is based on CRUST1.0
120 (Laske et al., 2012), which includes an average regional crustal thickness of around 8 km
121 (Fig. 2A), plus a 2.90 km thick water layer, which corresponds to the depth of the shallowest
122 OBS location (S11D). Deeper than 35km, it is based on ak135 (Kennett et al., 1995). Here,
123 ST and LT time windows of 0.2s and 10s are used, together with thresholds of 4 (trigger on)
124 and 1.5 (trigger off). This results in 1492 a priori events with 11399 P- and 13948 S-picks.
125
126 The P- and S- picks are refined manually and iteratively in combination with an update on the
127 1-D velocity model and the event locations. Event locations are computed using the
128 NonLinLoc package (Lomax et al., 2000). The package performs a probabilistic, non-linear
129 global-search inversion using the list of picked arrival times and a regional velocity model as
130 input. Following the probabilistic approach of Tarantola & Valette (1982) it calculates the
131 hypocentre location using the maximum likelihood of a probability density function of model
132 parameters in the temporal and spatial domain. The velocity model is updated using
133 VELEST3.1 (Kissling et al., 1994), which simultaneously inverts for 1-D P- and S-wave
134 velocities and hypocentral parameters. The velocity model has a substantial influence on the
135 depth accuracy, whereas lateral localisation of most earthquakes can be constrained even if
136 more general models are used. Further details can be found in Appendix 1.
137
138 Given this we perform an additional test to verify the robustness of the depth estimates. We
139 compare NonLinLoc solutions with different maximum search depth limits (15, 20, 25, 30
140 km, as well 200 km, which we will label as “no limit”). We use the following steps to
141 establish the preferred solution from the NonLinLoc testing with different maximum search
142 depth limits. Although the lateral locations are typically the same regardless of the depth

143 limit, we eliminate the few solutions where the lateral location of the event lies outside of
144 error of the rest of the locations (Fig. S1). We then choose the location that has the lowest
145 root mean square (RMS) error if it is outside of error from the remaining location solutions
146 (see Suppl. Fig. S1). For locations where results using multiple depth cut-offs are within error
147 of each other and shallower than 30 km we use the solution with the lowest RMS error. In
148 cases where the lowest RMS error is reached at > 30 km depth from the sea surface and the
149 solution is within error of a shallower solution, we favour a shallower solution, but we mark
150 the quality as marginal. We use 30 km depth as a cut-off because it corresponds to the
151 approximate depth of the 900 – 1000 ° isotherms from thermal models, which may be the
152 limit of predicted brittle deformation (Molnar, 2020; Kohli et al., 2021). Although locations
153 deeper than 30 km are generally unlikely, we will also present the deep solutions since deeper
154 hypocentres have been found in other locations (McGuire et al., 2012; Kuna et al., 2019; Yu
155 et al., 2021). To ensure the robustness of the computed depths are unbiased by
156 heterogeneities due to long raypaths, we also carried out tests using only the data from the
157 closest five stations with which an azimuthal gap below 180 degrees was still maintained. We
158 did this on a random sampling of 6 events ranging from M_L of 3.3 to 5.6. The locations
159 excluding longer paths were all within error of the original results.
160
161 For larger events, it is possible to carry out full moment tensor (MT) inversions, which gives
162 additional constraints on the depth accuracy (e.g., Braunmiller & Nábělek, 2008). We use the
163 Grond software tool (Heimann et al., 2018), which carries out a Bayesian bootstrap-based
164 inversion of the time-domain deviatoric MT. The data is filtered between 12.5 s and 25 s. For
165 solution stability reasons we focus on the depth location while keeping the previously
166 determined latitude and longitude information fixed. Our tests show that in general the same
167 epicentral locations are found within uncertainties. We estimate the quality of these

168 measurements based on the following parameters (Suppl. Figs. S2, S3): 1) the number of
169 stations for which the theoretical waveforms fit the data is high, we assign quality level "MT
170 best", respectively. If the fit is generally poorer and/or the number of stations with good fits
171 is low, we categorise the event as "MT fair". 2) The agreement of stacked radiation patterns
172 from different ensembles of stations (good agreement for best, overall agreement with
173 potential outliers for fair). All solutions show a depth constraint that is well defined. In all
174 cases where an MT solution exists, we use this depth estimate.
175
176 *Magnitudes*
177
178 We calculate local magnitudes for all the located earthquakes using amplitude measurements
179 of the picked P-arrivals. After demeaning and detrending the data, we remove the instrument
180 response and simulate the response of a Wood-Anderson seismometer. The data are then
181 filtered using a high-pass filter with a corner frequency of 4Hz to reduce oceanic noise. To
182 account for further noise we introduce a signal-to-noise threshold of 1.3 for the zero-to-peak
183 amplitude calculations that are used to compute local magnitudes. To account for changes in
184 recorded amplitude with hypocentral distance due to geometric spreading and anelastic
185 attenuation the event magnitudes are adjusted using the correction term:
186
187 $\mathrm{Log}_{10}(A) - M_{ISC} = -1.46\ \mathrm{Log}_{10}(r/100) - 0.0016\ (r - 100) - 6.2$
188
189 Here, A is the recorded amplitude, M_{ISC} is the magnitude as derived by the International
190 Seismological Centre (ISC), and r is the hypocentral distance. The term is derived similarly
191 to Abercrombie et al. (1996), using an empirical comparison to our MT solutions (Fig. 3).
192

193 *Magnitude-earthquake distribution*

194

195 The earthquake magnitude distribution can be described by the *b*-value, which is the gradient
196 of the Gutenberg-Richter relationship ($\mathrm{Log}\{N(M)\} = a - bM$; Gutenberg & Richter, 1944).
197 The relationship shows that the number of events (N) above a certain magnitude (M) can be
198 expressed by two positive constants, representing the overall seismic activity (a) and the
199 relative occurrence of small to large magnitude earthquakes (b).

200

201 To calculate the associated uncertainties we perform the maximum likelihood method (Aki
202 1965; Utsu 1965; Bender 1983) in combination with a Kolmogorov-Smirnov test. The
203 magnitude of completeness, M_C, is truncate at $M_c = 2.3$ to avoid large variations since they
204 can bias the results using a maximum likelihood calculation. The solution is accepted if the
205 magnitude distribution and the straight-line gradient b reach a similarity above M_C above a
206 predetermined significance level, in our case chosen to be more rigorous at 20% (Schlaphorst
207 et al., 2016).

208

209 **Results**

210

211 In total, 972 earthquakes could be located laterally (Fig. 4). Constraining depths with a larger
212 network spacing of around 40 km poses challenges in this setting. Still, we were able to
213 constrain depths for 928 events. 118 could be constrained by applying an MT inversion (Fig.
214 4B). Of the remaining event locations 650 are classified as good (Fig. 4C) and 150 are
215 classified marginal quality (Fig. 4D). The majority of the MT constrained events (88) are
216 located on the CTF and FZ. The lateral location uncertainty is smaller than depth uncertainty
217 with a median value of $\tilde{y} = 2.86$. Moment tensor solutions show the lowest depth

uncertainties with median values of $\tilde{z}$ = 5.42 km in comparison with the median NonLinLoc solutions for good ($\tilde{z}$ = 7.96 km) and marginal ($\tilde{z}$ = 11.87 km) categories (Fig. 4B, C, D). NonLinLoc hypocentres are better constrained inside the network with the following median values of $\tilde{y}$ = 2.39 km and $\tilde{z}$ = 8.36 km for CTF and $\tilde{y}$ = 15.09 km and $\tilde{z}$ = 24.81 km for RTF. Nearly all of the events are found on or close to the OTFs (793) and the MAR (155). Only a small number (10) are located on the inactive continuing FZs. Another 13 can be found off these features. Of the events located on or close to an OTF, 700 are close to the CTF, of which the majority is concentrated towards the eastern side, particularly clustered towards the ridge-transform intersection. A further 94 can be found around the RTF.

Earthquake depths, relative to sea level, determined from NonLinLoc, range from the seafloor to 43 km depth beneath the sea surface. Most (716) are located shallower than 15 km. Events on the MAR, away from the ridge-transform intersection, are mostly (36 out of 46) shallower than 10 km. Events on the MAR near the transform are deeper, with 12 events between 15 km and 30 km categorized as good. 60 events in the entire catalogue were located between 30 and 40 km depth, only 4 of which are classified as good and 56 as marginal. 14 are located at depths greater than 40 km and all categorised as marginal (Fig. 4D).

Most of the MT depths are well-constrained (96 out of 118; Fig. 5; Suppl. Figs. 2, 3). Most solutions (63) are characterised by probability density functions (pdfs) with a clear singular peak. Some solutions (35) have a more complex distribution, but the dominant peak is shallow (<20 km). We find 20 events where a deep (20 – 49 km) MT solution exists that fits the waveforms equally well or better than a shallower solution (<20 km) that we present for completeness (Fig. 6). The deep solutions are likely unrealistic, given the expected maximum depth of brittle deformation (Molnar, 2020; Kohli et al., 2021). Therefore, we favour the

243 shallower solution. In general, the deepest events are located along the CTF and RTF, while
244 the events beneath the MAR are shallower than 12 km below sea level. There is only one
245 event on the MAR that is deeper than 12 km. There is one intraplate earthquake with an MT
246 solution located on the African plate near the Chain FZ, with a depth of 18 km.
247
248 MT inversion of 118 events in our catalogue shows a mix of strike slip, normal and reverse
249 faults across the region (Fig. 5). Of the 88 focal mechanisms located on the CTF, the majority
250 shows right lateral strike-slip movement (39), mostly dipping to the north. Towards the
251 eastern end of the CTF, a combination of strike-slip and reverse faulting is observed (18).
252 Several reverse faulting mechanisms can be observed in some locations along the CTF as
253 well (20). Nearly all of the 29 MAR events show predominantly normal fault mechanisms
254 with a minor strike-slip component in some cases. Furthermore, a rotation of the normal
255 faulting axis can be observed close to ridge-transform intersections (Fig. 5; Suppl. Fig. S6).
256 The one intraplate event on the Chain FZ has a moment tensor which shows normal faulting
257 with fault plane solutions with north-south strike orientations
258
259 The local magnitudes from our catalogue range from 1.1 to 6.2. The local 6.2 magnitude is a
260 clipped estimate of the Romanche event, that was a larger Mw 7.1 in the global CMT
261 (Dziewonski et al., 1981; Ekström et al., 2012;) and in a detailed local study of the event
262 (Hicks et al., 2020). The local magnitude scale clips on this large event since it is outside of
263 our array with a small backazimuthal coverage. The next largest event in the catalogue is a
264 M_L 5.6 located on the CTF. We note that our relationship between amplitude and local
265 magnitude scale (Fig. 3) resembles one derived for the Azores (Gongóra et al., 2004), but
266 also to the continental setting of southern California (Hutton & Boore, 1987).
267

The moment magnitudes from MT inversion range from 3.0 to 6.2. This largest magnitude corresponds to the M_w 7.1 Romanche event (Hicks et al., 2020). The magnitude is vastly underestimated for three main reasons: 1) the large azimuthal gap, 2) the distance to the network, and 3) the usage of a CTF based velocity model and magnitude calibration. On the CTF three M_w>5 events were located, the largest being a M_w 5.6. The largest earthquake that we recorded on a MAR segment was a M_w 4.5, while the largest intraplate earthquake we recorded was a M_w 3.2.

The *b*-value for the CTF is 0.81 ± 0.09 and for the RTF is 0.76 ± 0.22. The network configuration results in large distances to the stations and azimuthal gaps for the events at the RTF, which leads to magnitude estimations being less well constrained. These factors combined with the lower number of detected events leads to higher uncertainties for events at RTF. In addition, the magnitude of completeness is larger outside the network at the RTF (M_C = 3.4) compared to inside the network at CTF (M_C = 2.3). The RTF also has larger median local magnitudes (M_L = 3.7) compared to the CTF (M_L = 2.4). Within the CTF the median local M_L values vary, with M_L = 2.5 in the west and M_L = 2.3 in the east.

Discussion

The results generally show an expected pattern of event distribution. They are mostly located close to the ridge-transform plate tectonic boundary between the African and South American Plates. The sub-ridge events are located at depths shallower than 12 km beneath sea level. These likely occur in the crust and the uppermost mantle assuming around 3 km average water depth at the ridge and a 6-7 km average crustal thickness (Christeson et al., 2019).

These can be explained through extension of the crust due to seafloor spreading. Earthquakes at slightly deeper depths than the crust beneath the ridge may occur given that geodynamic modelling suggests that lateral conductive cooling results in non-negligible thickness of the mantle lithosphere at slow spreading centres (Parmentier & Morgan, 1990). The deeper earthquakes observed in the transforms suggest that there is brittle deformation to deeper depths than beneath the ridges. The strain rate can be another component in controlling the depth extent of seismicity (Molnar, 2020). A deeper brittle-ductile transition beneath the transform in comparison to the ridges is predicted by simple thermal models. Brittle deformation in the mantle lithosphere has also been observed in teleseismic estimates for CTF and RTF (Abercrombie & Ekström, 2001).

The focal mechanisms along the plate boundary are also generally consistent with the ridge-transform system in the region. Specifically, we observed mostly normal fault MT solutions near the MAR segments, and mostly strike-slip solutions along the CTF and RTF consistent with the global view from the global CMT (Dziewonski et al., 1981; Ekström et al., 2012). The general pattern of north dipping focal mechanisms on the CTF is in agreement with previous results that are based solely on teleseismic observations (Abercrombie & Ekström, 2001). At the ridge-transform intersection we observe the rotation of the strike of the normal fault focal mechanism from ridge parallel on the ridge towards the strike direction of the OTF. This rotation reflects the transition in stress regime as the plate boundary transitions from spreading to transform fault tectonics (Fox and Gallo, 1984) as predicted by geodynamic modelling (Morgan & Parmentier, 1984). This also results in the observed arcuate shaped scarps bending in towards the transform faults in the ridge-transform intersection in the CTF (Harmon et al. 2018).

318 The presence of reverse fault MT solutions in some parts of the CTF is indicative of
319 transpression in the strike slip system. The reverse fault mechanisms are typically associated
320 with topographic highs within the CTF, which have been interpreted as positive flower
321 structures associated with restraining bends in the normal fault system (Harmon et al., 2018).
322 The four positive flower structures have visible sharp scarps in the bathymetry (Harmon et
323 al., 2018), and taken with the MT solutions, suggests that these are active features and the
324 CTF is in active transpression today. Transpression could be caused by a present-day rotation
325 and re-adjustment of the African-South American spreading system. Previously, it has been
326 suggested that the relative plate motions in the region have undergone a rotation of ~11°
327 anticlockwise based on observations of transpressional features on the major FZs to the north,
328 for example Romanche and St. Paul, (Bonatti et al., 1994; Maia et al., 2016). Our
329 observations support these notions and suggest that the change in motions is ongoing.
330
331 The cluster of intraplate seismicity (5 events) observed on the Chain FZ on the African Plate
332 at -11.5˚ longitude suggests there are internal stresses in the region of the earthquakes. The
333 MT solution indicates a relatively deep event (18 km) suggesting strain is accumulating in the
334 deeper part of the lithosphere caused brittle deformation there. The near vertical (or
335 horizontal) fault plane and north-south strike direction are at odds with the expected tectonic
336 fabric of the roughly east-west trending Chain FZ, so it does not appear to be re-activation of
337 the FZ. Another example of a large intraplate oceanic earthquake in the Wharton Basin in the
338 Indian Ocean was interpreted as FZ reactivation given that MT solutions were consistent with
339 the FZ orientations (Yue et al., 2012), and the event may have been related to the nearby
340 Sumatran subduction zone. One explanation for our event is that the intraplate stresses are
341 due to the aforementioned rotation of the relative plate motions (Bonatti et al., 1994; Maia et
342 al., 2016). However, it is unclear whether the observed focal mechanism would be consistent

with this interpretation. Another potential explanation of intraplate stress in the region may be due to ocean mantle dynamics. Surface wave tomography and magnetotelluric imaging across the PI-LAB region image a high velocity and high resistivity in this region centred at 10.5˚W longitude and 0˚N latitude with shear velocities of greater than 4.4 km/s and $\log_{10}$ (resistivities) > 1.5 extending from 30 to 100 km depth that was interpreted as a lithospheric drip (Harmon et al., 2020; 2021; Wang et al., 2020). The lack of an observed receiver function phase from the lithosphere-asthenosphere boundary in this location was interpreted as either the absence of melt ponding beneath the plate and/or strong lithosphere-asthenosphere topography, again consistent with a drip (Rychert et al., 2021). The observed vertical MT motion of the large event recorded in this region may be consistent with the vertical stresses of the downwelling lithosphere (Fig. 5).

Events beneath the CTF are located deeper than the predicted depth of the 600˚C isotherm from half-space cooling, i.e., a greater depth than the previously proposed limit of seismic slip at 600˚C based on teleseismic observations (Abercrombie & Ekström, 2001) and earthquake rupture experiments (Boettcher et al., 2007). Earthquakes deeper than expected based on isotherms predicted for an oceanic transform from the half space cooling model have also been observed at Blanco (Kuna et al., 2019), Gofar (McGuire et al., 2012) and Romanche (Yu et al., 2021). These observations are typically interpreted as lithospheric cooling caused by hydrothermal circulation, which can deepen the depth of the brittle-ductile transition (Roland et al., 2010). In some cases, the events were deeper than expected by numerical modelling accounting for hydrothermal circulation (Roland et al., 2010; McGuire et al., 2012; Kuna et al., 2019). Therefore, an alternative explanation that was suggested based on exhumed hydraulically altered mylonites is that brittle and ductile deformation can occur over a broad range of temperatures (300˚C – 900˚/1000˚C) and, therefore, a broad

range of depths, owing to variable seawater infiltration and grain sizes along the fault (Molnar, 2020; Kohli et al., 2021).

The *b*-value of the entire catalogue of CTF events is lower than the global average value of 1.0 but in agreement with other studies in the region (Leptokaropoulos et al, 2021). The low *b*-value (0.81 ± 0.09) also supports the notion that average coupling along the CTF is low and that much of the strain is accommodated aseismically. However, historical seismicity, which has resulted in several large events (Mw > 6.5), suggests that coupling in discrete locations may be higher (Shi et al., 2021). This agrees with results from Blanco Transform, where crustal *b*-values are similarly low ($b = 0.78 \pm 10$) and coupling is low but variable along the fault (Kuna et al., 2019).

We compare the cumulative moment release over the 1-year of our array to examine the average seismic coupling. We find that the cumulative moment release on the CTF was 4.9 x 10^{17} Nm. The release on the RTF was 5.7 x 10^{19} Nm. The release on the ridge segments had a cumulative moment of 3.3 x 10^{16} Nm. The higher release on the Romanche is due to the M_w 7.1 event and its aftershock sequence. A more detailed investigation of this event is presented in (Hicks et al., 2020). The predicted moment release per year for the thermal lithosphere from Boettcher and Jordan, (2004) for the CTF is 5.9 x 10^{18} Nm yr^{-1}, which suggests only ~1% of the predicted moment release was released seismically over the year-long observation period. Our results also support the notion that the CTF is relatively weak and not coupled. For the entire Romanche, the predicted value of cumulative moment release from the thermal lithosphere is 2.9 x 10^{19} Nm yr^{-1}, approximately half of the observed moment release. Large events like the M_w 7.1 occur relatively rarely, approximately every 30 years on Romanche, indicating the moment release during this time was particularly high. Given that these large

393 events occur on different segments, and do not rupture the entire length of the transform fault,
394 portions of the RTF likely have high seismic coupling. This observation also highlights the
395 temporal variability of moment release on OTFs. The MAR segments show a very low
396 cumulative moment (3.3×10^{16} Nm) compared to the OTFs (>=4.9×10^{17} Nm) in the region
397 for the duration of the deployment, which may suggest that the normal faulting also has a low
398 coupling during this time period.
399
400 **Conclusions**
401
402 We present an earthquake catalogue from a broadband ocean bottom seismic experiment
403 from March 2016 to March 2017 at the equatorial MAR centred around the Chain FZ, which
404 provides one of the first detailed seismicity study from a larger local network around a slow
405 moving OTF. Most of the events are located on the South American – African Plate boundary
406 as expected although we also recorded 10 events near the Chain FZ, east of the OTF and 13
407 additional intraplate earthquakes. Focal mechanisms on the MAR are predominantly
408 characterised as normal faulting and on the OTF they are predominantly strike slip as
409 expected. A few (17) predominantly reverse faulting mechanisms on the transform are likely
410 caused by a transpressional stress regime related to current rotation of the ridge-transform
411 system. The focal mechanism of an intraplate event on the FZ shows vertical displacement,
412 consistent with a hypothesized nearby lithospheric drip. The magnitudes range from 1.1 to
413 5.6 and we find a *b*-value of 0.81 ± 0.09 for the CTF. The earthquakes on the ridge are
414 limited to crust and shallowest mantle (< 12 km depth) while the events on the CTF are
415 deeper, with high quality MT location depths of up to 26 km beneath the sea surface, which is
416 much deeper than the depth of the brittle-ductile transition predicted for simple thermal
417 models. These deeper events are likely linked to the effects of hydrothermal circulation.
418

Acknowledgements

All images were produced using GMT (Wessel et al., 2013). Additional information about SDX can be found at www.liv.ac.uk/~aeh/index.html. D.S. would like to acknowledge the financial support FCT through project UIDB/50019/2020 – IDL.

D.S. managed the study and carried out the locating. C.A.R. and N.H. conceived the experiment, acquired funding, managed the project, and contributed to the manuscript. S.P.H. created the initial automated detection of events, assisted with the locations, and commented on the manuscript. P.B. worked on event depth improvements and commented on the manuscript. J.M.K. co-managed the project and commented on the manuscript. R.E.A. contributed to improving the event localization method and commented on the manuscript.

Data Availability

The continuous raw seismic waveform data from the PI-LAB OBS network is available to download from IRIS Data Management Center (https://doi.org/10.7914/SN/XS_2016).

Appendix 1 – Details on iterative pick refinement, model update and event localisation in NonLinLoc

In step 1, P- and S-arrivals are readjusted using the vertical component and the Seismic Analysis Code (SAC). This is done without the implementation of calculated theoretical arrival times derived from the automated picks in order to keep the reassessed picks unbiased. Although different filters as well as the unfiltered data are used to evaluate potential onsets, we use the same corner frequencies to determine the onsets to have consistent P- and S-moveouts and P-to-S travel time differences. The weighting of picks is assigned to reflect their quality, using levels from 0 (highest) to 4 (lowest). The levels are associated with an

443 uncertainty in arrival time, using values of 0.1s, 0.2s, 0.5s, 0.8s, and 1.5s (Hicks et al., 2014).
444 Picks of quality level 4 are subsequently omitted from the locating process.
445
446 In step 2, the event locations are computed using the NonLinLoc package (Lomax et al.,
447 2000). The package performs a probabilistic, non-linear global-search inversion using the list
448 of picked arrival times and a regional velocity model as input. Following the probabilistic
449 approach of Tarantola & Valette (1982) it calculates the hypocentre location using maximum
450 likelihood of a probability density function of model parameters in the temporal and spatial
451 domain. The initial velocity model is given by CRUST1.0 resulting in an average regional
452 crustal thickness of around 8 km (Fig. 2A), plus a 2.90 km thick water layer, which
453 corresponds to the depth of the shallowest OBS location (S11D). We do not include a
454 sediment layer since it is supposed to be very thin in the area (Agius et al., 2018; Saikia et al.,
455 2020). In this step, we also combine picks that are counted as multiple events by the
456 STA/LTA detector, thus reducing the overall number of events.
457
458 A minimum of 3 stations with clearly observable and coherent arrivals is required to identify
459 the event. We use a search grid spacing of 1km in all three dimensions and an average v_P/v_S
460 ratio of 1.73, based on picked P–S arrival time differences (Fig. 2B). The quality of the
461 resulting location is based on temporal uncertainty (i.e., root mean square or RMS error) as
462 well as spatial uncertainty. The latter is a combination of the size of the ellipsoidal
463 approximation to the 1σ confidence level of the location likelihood scatter and the overall
464 shape of the scatter sample. Lateral localisation of most earthquakes can be constrained
465 relatively precisely, even if more general models are used, whereas the velocity model has a
466 larger impact on depth localisation.
467

In step 3, the picks of events with low quality are refined. This includes all events that either have large location uncertainty and/or where picks and theoretical arrival times show large mismatches. Here we use the Seismic Data eXplorer (SDX; Hicks et al., 2014), additionally including the two horizontal components and the hydrophone component. SDX updates theoretical onset time calculations of P- and S-phases automatically after each change of pick placement. In general, this reduces the number of mispicks. There are, however, instances, where clearly identifiable onsets do not match the theoretical arrivals. In most cases, this is due to an inaccurate velocity model.

In step 4, the velocity model is updated, based on the updated set of picks. We use the program VELEST3.1 (Kissling et al., 1994), which simultaneously inverts for 1D P- and S-wave velocities and hypocentral parameters. For this step, we concentrate on the picks of events on or close to the CTF. This ensures good azimuthal coverage with a gap of less than 180˚. Also, regional heterogeneities are likely to distort a uniform velocity model if the area is chosen too large and diverse. We limit the selection further to events with an RMS of less than 1.2, a minimum number of P-picks of 5, and a minimum number of S picks of 3.

Steps 2, 3 and 4 are run iteratively until the model and arrival time picks stabilise. Here, three iterations proved to be sufficient.

488 **References**

489 Abercrombie, R. E. (1996). The magnitude-frequency distribution of earthquakes recorded
490 with deep seismometers at Cajon Pass, southern California. Tectonophysics, 261(1-3), 1-7.
491 DOI: 10.1016/0040-1951(96)00052-2.
492
493 Abercrombie, R. E., & Ekström, G. (2001). Earthquake slip on oceanic transform faults.
494 Nature, 410(6824), 74-77. DOI: 10.1038/35065064.
495
496 Agius, M. R., N. Harmon, C. A. Rychert, S. Tharimena, and J. M. M. Kendall (2018),
497 Sediment characterization at the equatorial Mid-Atlantic Ridge from P-to-S teleseismic phase
498 conversions recorded on the PI-LAB experiment, Geophys. Res. Lett., 45, 12,244–12,252.
499 DOI: 10.1029/2018GL080565.
500
501 Amante, C., & Eakins, B. W. (2009). ETOPO1 arc-minute global relief model: procedures,
502 data sources and analysis. DOI: 10.7289/V5C8276M.
503
504 Bakun, W. H., & Joyner, W. B. (1984). The M_L scale in central California. Bulletin of the
505 Seismological Society of America, 74(5), 1827-1843. DOI: 10.1785/BSSA0740051827
506
507 Baumbach, M., Bindi, D., Grosser, H., Milkereit, C., Parolai, S., Wang, R., ... & Zschau, J.
508 (2003). Calibration of an ML scale in northwestern Turkey from 1999 Izmit aftershocks.
509 Bulletin of the Seismological Society of America, 93(5), 2289-2295. DOI:
510 10.1785/0120020157
511

512 Bird, P. (2003). An updated digital model of plate boundaries. Geochemistry, Geophysics,
513 Geosystems, 4(3). DOI: 10.1029/2001GC000252
514
515 Boettcher, M. S., Hirth, G., & Evans, B. (2007). Olivine friction at the base of oceanic
516 seismogenic zones. Journal of Geophysical Research: Solid Earth, 112(B1). DOI:
517 10.1029/2006JB004301
518
519 Boettcher, M. S., & Jordan, T. H. (2004). Earthquake scaling relations for mid□ocean ridge
520 transform faults. Journal of Geophysical Research: Solid Earth, 109(B12). DOI:
521 10.1029/2004JB003110
522
523 Bogiatzis, P., Karamitrou, A., Ward Neale, J., Harmon, N., Rychert, C. A., & Srokosz, M.
524 (2020). Source regions of infragravity waves recorded at the bottom of the equatorial Atlantic
525 Ocean, using OBS of the PI□LAB experiment. Journal of Geophysical Research: Oceans,
526 125(6), e2019JC015430. DOI: 10.1029/2019JC015430
527
528 Bonatti, E., Ligi, M., Gasperini, L., Peyve, A., Raznitsin, Y. U., & Chen, Y. J. (1994).
529 Transform migration and vertical tectonics at the Romanche fracture zone, equatorial
530 Atlantic. Journal of Geophysical Research: Solid Earth, 99(B11), 21779-21802. DOI:
531 10.1029/94JB01178
532
533 Braunmiller, J., & Nábělek, J. (2008). Segmentation of the Blanco Transform Fault Zone
534 from earthquake analysis: Complex tectonics of an oceanic transform fault. Journal of
535 Geophysical Research: Solid Earth, 113(B7). DOI: 10.1029/2007JB005213
536

Christeson, G. L., J. A. Goff, and R. S. Reece (2019), Synthesis of Oceanic Crustal Structure From Two-Dimensional Seismic Profiles, Reviews of Geophysics, 57(2), 504-529. DOI:10.1029/2019RG000641.

DeMets, C., Gordon, R. G., Argus, D. F., & Stein, S. (1994). Effect of recent revisions to the geomagnetic reversal time scale on estimates of current plate motions. Geophysical research letters, 21(20), 2191-2194. DOI: 10.1029/94GL02118

Dziewonski, A. M., T.-A. Chou and J. H. Woodhouse, Determination of earthquake source parameters from waveform data for studies of global and regional seismicity, J. Geophys. Res., 86, 2825-2852, 1981. DOI:10.1029/JB086iB04p02825

Ekström, G., M. Nettles, and A. M. Dziewonski, The global CMT project 2004-2010: Centroid-moment tensors for 13,017 earthquakes, Phys. Earth Planet. Inter., 200-201, 1-9, 2012. DOI:10.1016/j.pepi.2012.04.002

Fox, P. J., & Gallo, D. G. (1984). A tectonic model for ridge-transform-ridge plate boundaries: Implications for the structure of oceanic lithosphere. Tectonophysics, 104(3-4), 205-242. DOI: 10.1016/0040-1951(84)90124-0

Góngora, E., Carrilho, F., & Oliveira, C. S. (2004). Calibration of local magnitude ML in the Azores archipelago based on recent digital recordings. Pure and Applied Geophysics, 161(3), 647-659. DOI: 10.1007/s00024-003-2467-0

561 Gregory, E. P., Singh, S. C., Marjanović, M., & Wang, Z. (2021). Serpentinized peridotite
562 versus thick mafic crust at the Romanche oceanic transform fault. Geology, 49(9), 1132-
563 1136. DOI: 10.1130/G49097.1
564
565 Gutenberg, B. and Richter, C.E, 1944. Frequency of earthquakes in California. Bull. Seismol.
566 Soc. Am., 34: 185-188. DOI: 10.1785/BSSA0340040185
567
568 Harmon, N., Rychert, C., Agius, M., Tharimena, S., Le Bas, T., Kendall, J. M., & Constable,
569 S. (2018). Marine geophysical investigation of the chain fracture zone in the Equatorial
570 Atlantic from the PI□LAB experiment. Journal of Geophysical Research: Solid Earth,
571 123(12), 11-016. DOI: 10.1029/2018JB015982.
572
573 Harmon, N., C. A. Rychert, J. M. Kendall, M. Agius, P. Bogiatzis, and S. Tharimena (2020),
574 Evolution of the oceanic lithosphere in the equatorial Atlantic from Rayleigh wave
575 tomography, evidence for small□scale convection from the PI□LAB experiment, Geochem.
576 Geophys. Geosys., 21, e2020GC009174.
577
578 Heimann, S., Isken, M., Kühn, D., Sudhaus, H., Steinberg, A., Daout, S., Cesca, S., Bathke,
579 H., Dahm, T. (2018). Grond: a probabilistic earthquake source inversion framework,
580 Potsdam: GFZ Data Services. DOI:10.5880/GFZ.2.1.2018.003
581
582 Hicks, S. P., Rietbrock, A., Ryder, I. M., Lee, C. S., & Miller, M. (2014). Anatomy of a
583 megathrust: The 2010 M8. 8 Maule, Chile earthquake rupture zone imaged using seismic
584 tomography. Earth and Planetary Science Letters, 405, 142-155. DOI:
585 10.1016/j.epsl.2014.08.028.

Hicks, S. P., Okuwaki, R., Steinberg, A., Rychert, C. A., Harmon, N., Abercrombie, R. E., … & Sudhaus, H. (2020). Back-propagating supershear rupture in the 2016 M_W 7.1 Romanche transform fault earthquake. Nature Geoscience, 13(9), 647-653. DOI: 10.1038/s41561-020-0619-9

Hutton, L. K., & Boore, D. M. (1987). The M_L scale in southern California. Bulletin of the Seismological Society of America, 77(6), 2074-2094. DOI: 10.1785/BSSA0770062074

Illsley□Kemp, F., Keir, D., Bull, J. M., Ayele, A., Hammond, J. O., Kendall, J. M., ... & Goitom, B. (2017). Local earthquake magnitude scale and b□value for the Danakil region of northern Afar. Bulletin of the Seismological Society of America, 107(2), 521-531. DOI: 10.1785/0120150253.

Kennett, B.L.N. Engdahl, E.R. & Buland R., 1995. Constraints on seismic velocities in the Earth from travel times, Geophys J Int, 122, 108-124. DOI: 10.1111/j.1365-246X.1995.tb03540.x.

Kissling, E., W.L. Ellsworth, D. Eberhart-Phillips, and U. Kradolfer (1994). Initial reference models in local earthquake tomography, J. Geophys. Res., 99, 19635-19646. DOI: 10.1029/93JB03138

Kohli, A., Wolfson-Schwehr, M., Prigent, C., & Warren, J. M. (2021). Oceanic transform fault seismicity and slip mode influenced by seawater infiltration. Nature Geoscience, 14(8), 606-611. DOI: 10.1038/s41561-021-00778-1

Kuna, V. M., Nábělek, J. L., & Braunmiller, J. (2019). Mode of slip and crust–mantle interaction at oceanic transform faults. Nature Geoscience, 12(2), 138-142. DOI: 10.1038/s41561-018-0287-1

Langston, C. A., Brazier, R., Nyblade, A. A., & Owens, T. J. (1998). Local magnitude scale and seismicity rate for Tanzania, East Africa. Bulletin of the Seismological Society of America, 88(3), 712-721. DOI: 10.1785/BSSA0880030712

Laske, G., Masters., G., Ma, Z. and Pasyanos, M., Update on CRUST1.0 – A 1-degree Global Model of Earth's Crust, Geophys. Res. Abstracts, 15, Abstract EGU2013-2658, 2013.

Leptokaropoulos, K., Harmon, N., Hicks, S. P., Rychert, C. A., Schlaphorst, D., & Kendall, J. M. (2021). Tidal Triggering of Microseismicity at the Equatorial Mid□Atlantic Ridge, Inferred From the PI□LAB Experiment. Journal of Geophysical Research: Solid Earth, 126(9), e2021JB022251. DOI: 10.1029/2021JB022251

Lomax, A., J. Virieux, P. Volant and C. Berge, (2000), Probabilistic earthquake location in 3D and layered models: Introduction of a Metropolis-Gibbs method and comparison with linear locations, in Advances in Seismic Event Location, Thurber, C.H., and N. Rabinowitz (eds.), Kluwer, Amsterdam, 101-134. DOI: 10.1007/978-94-015-9536-0_5

Maia, M., Sichel, S., Briais, A., Brunelli, D., Ligi, M., Ferreira, N., ... & Oliveira, P. (2016). Extreme mantle uplift and exhumation along a transpressive transform fault. Nature Geoscience, 9(8), 619-623. DOI: 10.1038/ngeo2759

McGuire, J. J., Collins, J. A., Gouédard, P., Roland, E., Lizarralde, D., Boettcher, M. S., ... & Van Der Hilst, R. D. (2012). Variations in earthquake rupture properties along the Gofar transform fault, East Pacific Rise. Nature Geoscience, 5(5), 336-341. DOI: 10.1038/ngeo1454

Molnar, P. (2020). The brittle□plastic transition, earthquakes, temperatures, and strain rates. Journal of Geophysical Research: Solid Earth, 125(7), e2019JB019335. DOI:

Morgan, J. P., & Parmentier, E. M. (1984). Lithospheric stress near a ridge□transform intersection. Geophysical Research Letters, 11(2), 113-116. DOI: 10.1029/GL011i002p00113

Müller, R. D., Sdrolias, M., Gaina, C., & Roest, W. R. (2008). Age, spreading rates, and spreading asymmetry of the world's ocean crust. Geochemistry, Geophysics, Geosystems, 9(4). DOI: 10.1029/2007GC001743.

Ottemöller, L., & Sargeant, S. (2013). A local magnitude scale ML for the United Kingdom. Bulletin of the Seismological Society of America, 103(5), 2884-2893. DOI: 10.1785/0120130085

Parmentier, E. M., & Morgan, J. P. (1990). Spreading rate dependence of three-dimensional structure in oceanic spreading centres. Nature, 348(6299), 325-328. DOI: 10.1038/348325a0

Richter, C. F. (1935). An instrumental earthquake magnitude scale, Bull. Seism. Soc. Am. 25, 1-31. DOI: 10.1785/BSSA0250010001

Richter, C. F. (1958). Elementary Seismology, W. H. Freeman and Co., San Francisco, California, 578 pp.

Roland, E., Behn, M. D., & Hirth, G. (2010). Thermal□mechanical behavior of oceanic transform faults: Implications for the spatial distribution of seismicity. Geochemistry, Geophysics, Geosystems, 11(7). DOI: 10.1029/2010GC003034

Rychert, C. A., Tharimena, S., Harmon, N., Wang, S., Constable, S., Kendall, J. M., ... & Schlaphorst, D. (2021). A dynamic lithosphere–asthenosphere boundary near the equatorial Mid-Atlantic Ridge. Earth and Planetary Science Letters, 566, 116949. DOI: 10.1016/j.epsl.2021.116949

Saikia, U., C. Rychert, N. Harmon and J.M. Kendall (2020), Sediment structure at the equatorial mid atlantic ridge constrained by seafloor admittance using data from the PI LAB experiment, Mar. Geophys. Res., 41, 3, doi: 10.1007/s11001-020-09402-0

Saikia, U., C. Rychert, N. Harmon, and J. M. Kendall (2021), Upper mantle anisotropic shear velocity structure at the equatorial Mid-Atlantic ridge constrained by Rayleigh wave group velocity analysis from the PI-LAB experiment, Geochem. Geophys. Geosys., 22, e2020GC009495, DOI: 10.1029/2020GC009495

Saunders, I., Ottemöller, L., Brandt, M. B., & Fourie, C. J. (2013). Calibration of an ML scale for South Africa using tectonic earthquake data recorded by the South African National

685 Seismograph Network: 2006 to 2009. Journal of seismology, 17(2), 437-451. DOI:
686 10.1007/s10950-012-9329-0
687
688 Schlaphorst, D., Kendall, J. M., Collier, J. S., Verdon, J. P., Blundy, J., Baptie, B., ... &
689 Bouin, M. P. (2016). Water, oceanic fracture zones and the lubrication of subducting plate
690 boundaries—insights from seismicity. Geophysical Journal International, 204(3), 1405-1420.
691 DOI: 10.1093/gji/ggv509.
692
693 Schorlemmer, D., Wiemer, S., & Wyss, M. (2005). Variations in earthquake-size distribution
694 across different stress regimes. Nature, 437(7058), 539-542. DOI: 10.1038/nature04094.
695
696 Shi, P., Meng W. & Pockalny, R. The ubiquitous creeping segments on oceanic transform
697 faults, Geology 50, 199-204 (2021). DOI: 10.1130/G49562.1
698
699 Slemmons, D. B., & Depolo, C. M. (1986). Evaluation of active faulting and associated
700 hazards. Active Tectonics, 1986, 45-62.
701
702 Tarantola, A. and Valette, B., 1982, Inverse problems = quest for information., J. Geophys.,
703 50, 159-170.
704
705 Wang, S., Constable, S., Rychert, C. A., & Harmon, N. (2020). A lithosphere□asthenosphere
706 boundary and partial melt estimated using marine magnetotelluric data at the central Middle
707 Atlantic Ridge. Geochemistry, Geophysics, Geosystems, 21(9), e2020GC009177. DOI:
708 10.1029/2020GC009177
709

Wessel, P., W. H. F. Smith, R. Scharroo, J. Luis, and F. Wobbe, Generic Mapping Tools: Improved Version Released, EOS Trans. AGU, 94(45), p. 409–410, 2013. DOI:10.1002/2013EO450001.

Yu, Z., Singh, S. C., Gregory, E. P., Maia, M., Wang, Z., & Brunelli, D. (2021). Semibrittle seismic deformation in high-temperature mantle mylonite shear zone along the Romanche transform fault. Science Advances, 7(15), eabf3388. DOI: 10.1126/sciadv.abf3388

Yue, H., T. Lay, and K. D. Koper (2012), En échelon and orthogonal fault ruptures of the 11 April 2012 great intraplate earthquakes, Nature, 490(7419), 245-249. DOI:10.1038/nature11492.

Tables

Tab. 1: PI-LAB network OBS station details. Stations indicated with an asterisk were not used. Except for L27A running time is equivalent to deployment time.

Station	Lon	Lat	Depth (m)	Running Time	Notes
I01D*	-17.8855	1.2734	-4047	N/A	*unrecovered*
L02A	-17.4085	-1.1667	-3499	06/03/2016 – 24/03/2017	*did not level*
S03D	-17.0315	-2.4021	-3750	05/03/2016 – 25/03/2017	
I04D	-16.1733	-2.1238	-3928	07/03/2016 – 24/03/2017	
L05A	-15.4058	-1.8577	-4052	07/03/2016 – 21/03/2017	*stopped after 150 days*
S06D	-14.4298	-1.6703	-3778	06/03/2016 – 19/03/2017	
I07D	-14.0428	-1.5565	-3819	08/03/2016 – 22/03/2017	
L08D*	-13.6409	-1.4493	-3357	08/03/2022 – 18/03/2017	*only 1 horizontal channel*
L09A	-13.3185	-1.3569	-3378	08/03/2016 – 18/03/2017	*1 flat horizontal channel*
S10D	-12.9697	-1.3180	-3015	07/03/2016 – 18/03/2017	
S11D	-12.4602	-1.1691	-2905	07/03/2016 – 18/03/2017	
I12D	-10.7766	-0.8683	-4022	19/03/2016 – 17/03/2017	
L13D	-9.5619	-0.5862	-4659	09/03/2016 – 16/03/2017	*usable data until 23/12/16*
I14D	-7.9524	-0.3522	-4702	10/03/2016 – 10/03/2017	
S15D	-6.6228	0.1814	-4927	09/03/2016 – 16/03/2017	*rocking, some bad data*
L16D	-7.8953	0.8933	-4581	11/03/2016 – 15/03/2017	*usable data until 24/02/16*
S17D	-8.5121	0.7422	-5205	09/03/2016 – 15/03/2017	
L18D	-9.3765	0.5769	-4890	11/03/2016 – 14/03/2017	
S19D	-9.9754	0.4809	-4607	10/03/2016 – 14/03/2017	
I20D	-10.5352	0.3681	-4724	12/03/2016 – 13/03/2017	
L21D	-11.0380	0.2364	-4625	11/03/2016 – 13/03/2017	
S22D	-11.6799	0.1254	-4352	10/03/2016 – 13/03/2017	
L23D*	-12.1478	0.0521	-4631	12/03/2016 – 12/03/2017	*timing issues*
S24D	-12.7806	-0.1383	-4453	10/03/2016 – 13/03/2017	
L25D*	-13.2230	-0.1745	-4207	12/03/2022 – 11/03/2017	*disk failure*
S26D	-13.6260	-0.3434	-4216	11/03/2016 – 12/03/2017	
L27A*	-13.9427	-0.4007	-3928	12/03/2016 – 23/08/2016	*1 flat horizontal channel*
I28D	-14.2684	-0.4918	-3711	13/03/2016 – 11/03/2017	
S29D	-14.6272	-0.5597	-3626	11/03/2016 – 11/03/2017	
L30A	-14.9467	-0.5880	-4003	13/03/2016 – 10/03/2017	
S31D	-15.3188	-0.7141	-3408	11/03/2016 – 11/03/2017	
S32D	-15.6470	-0.7968	-2967	11/03/2016 – 11/03/2017	
L33D	-16.0152	-0.8747	-3919	13/03/2016 – 09/03/2017	
I34D	-16.3485	-0.9579	-2964	14/03/2016 – 09/03/2017	
S35D*	-16.6798	-1.0372	-3773	11/03/2016 – 11/03/2017	*disk failure*
I36D*	-17.0306	-1.1170	-3938	N/A	*unrecovered*
L37D	-14.9718	1.5657	-5054	19/03/2016 – 08/03/2017	
S38D	-12.7623	1.9218	-4926	18/03/2016 – 08/03/2017	
L39D*	-11.4904	2.0557	-4685	20/03/2016 – 07/03/2017	*unrecovered*

Figures

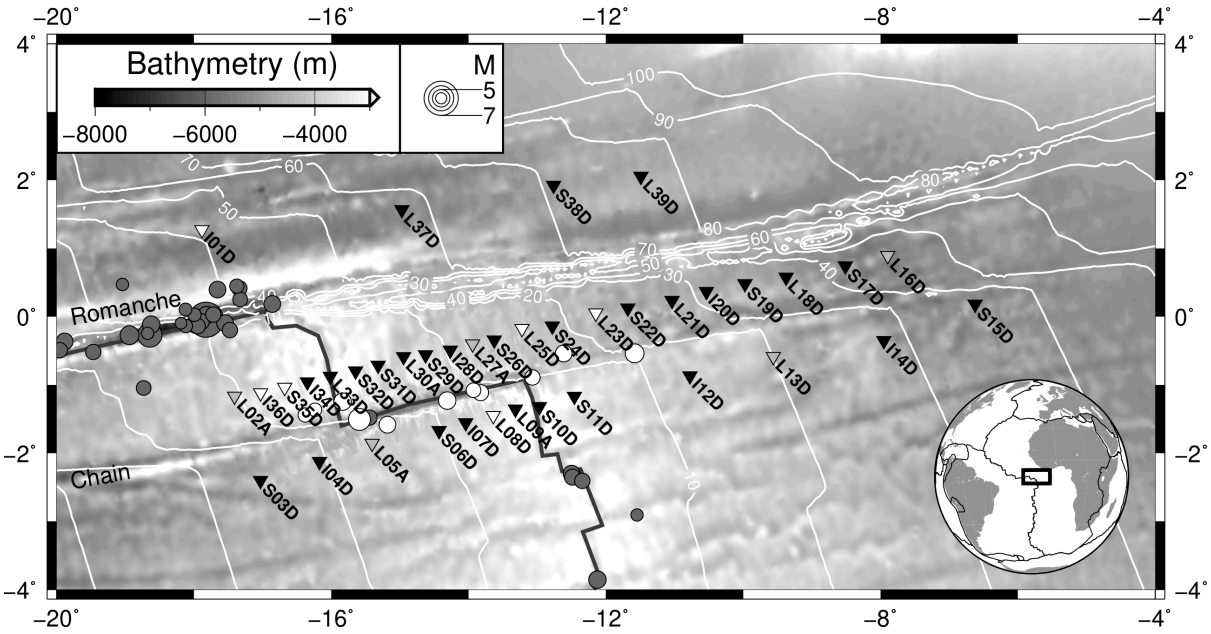

Fig. 1: Map of the study area (see inset for global context), including the PI-LAB station network. Some stations did not provide usable data for the entire timespan of the experiment (white triangles), some stations were only returning useful data for parts of the deployment (grey triangles); see details in Table 1. Events from the ISC during the time of the deployment are shown by circles, events around the CTF (white circles) have been used to calibrate the local event magnitude (see Fig. 3). In the global catalogue, all of these events have been assigned default depth values of 10km. Bathymetry data is taken from ETOPO1 (Amante & Eakins, 2009) with an additional higher resolution image around the CTF (Harmon et al., 2018. The thick solid line denotes the MAR location (adapted from Bird, 2003). White thin lines show age contours in Ma (Müller et al, 2008).

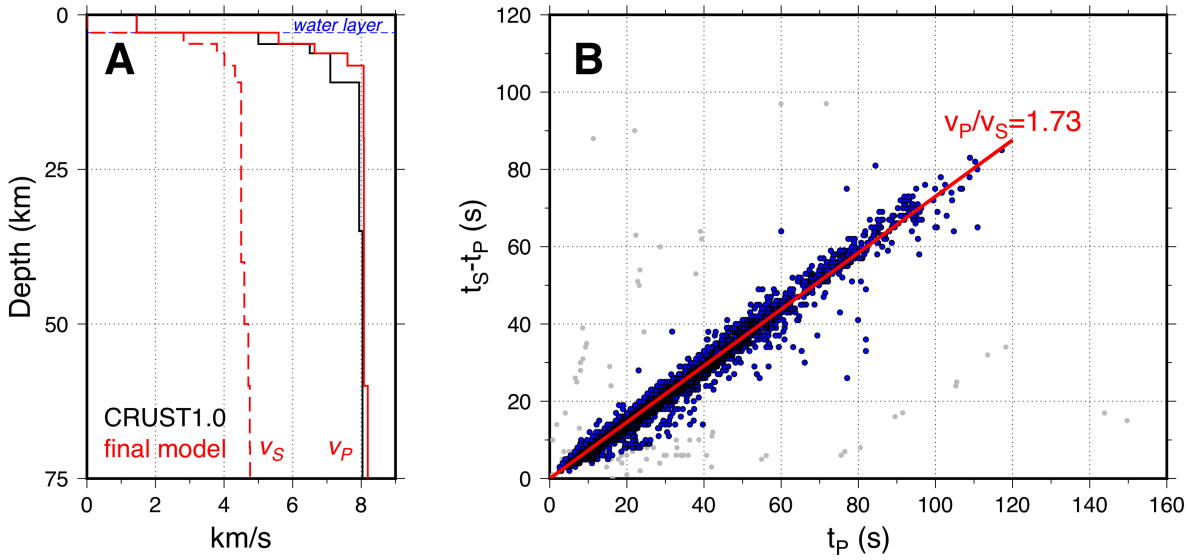

781

782 Fig. 2: (A) Initial (CRUST1.0) and final 1-D velocity-depth models. Note that CRUST1.0

783 only provides a P-velocity model. (B) Wadati plot of P- and S- arrival time picks (7345 pairs)

784 for all events. The red line shows the average v_P/v_S value of 1.73. About 98.1% (7206 pairs in

785 blue) fall within ± 0.4 of that value, about 83.7% (6146 pairs) fall within ± 0.1.

786

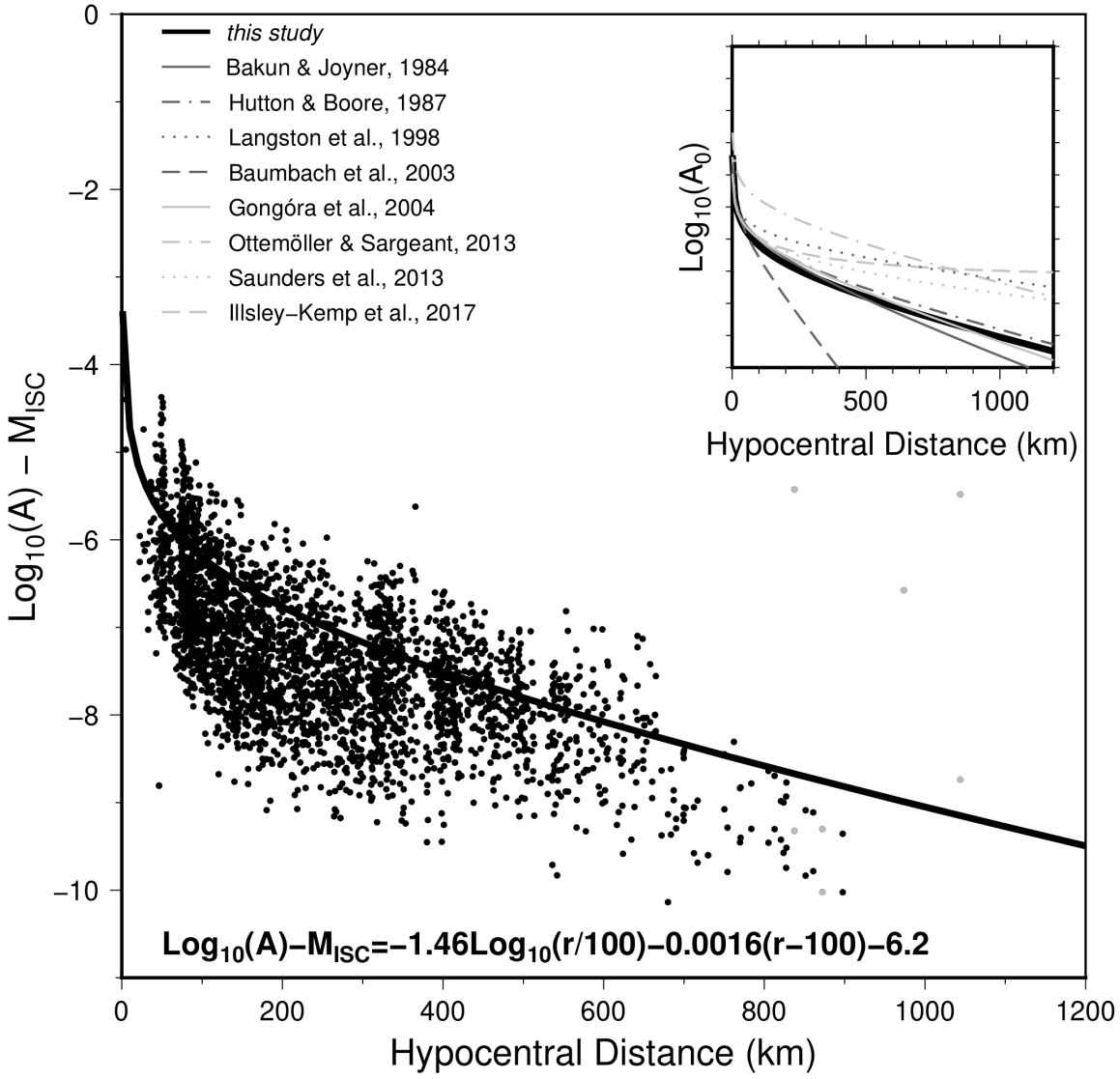

787

788 Fig. 3: Magnitude calibration with MT inversion solutions. Note, that results from station
789 S15D (grey dots) are taken out of the calculation, since the instrument was located on a slope
790 rocking and produced erroneous data. The inset shows different correction curves, all shifted
791 to match the original setup by Richter (1935, 1958).

792

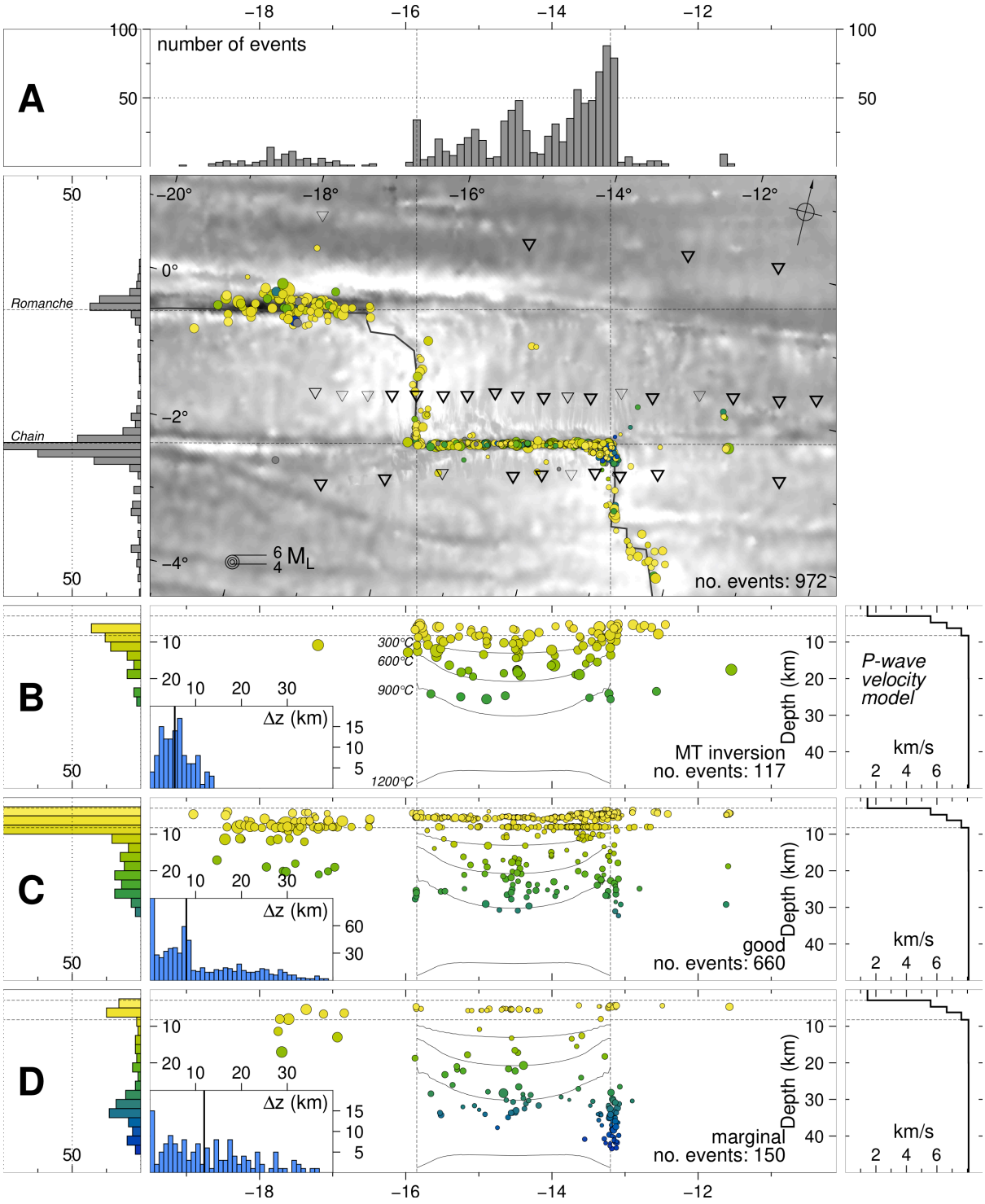

Fig. 4: Catalogue event location and magnitude results. (A) Map showing the epicentres coloured by depth. Top and left panels show histograms by projected longitude and latitude. (B-D) Cross section along the CTF and FZ. Depth uncertainties are shown in the blue histograms with the median value being depicted by vertical black lines. For clarity, error bars have been omitted from the figure but can be seen in Supplementary Figure S4. Events

799 are divided by quality (B: events for which moment tensor inversion was possible; C: good
800 locating results with NonLinLoc; D: marginal locating results with NonLinLoc) Isotherms
801 (300 – 1200˚C in steps of 300˚C) from a half space cooling model (using the lower half
802 spreading rate from the African plate, 15.7mm/yr, which results in deeper isotherms) are also
803 shown along the CTF. Also shown are depth histograms (left) and the final P-velocity model
804 (right). See Figure 1 for further details. See Supplementary Table S1 for event details.
805

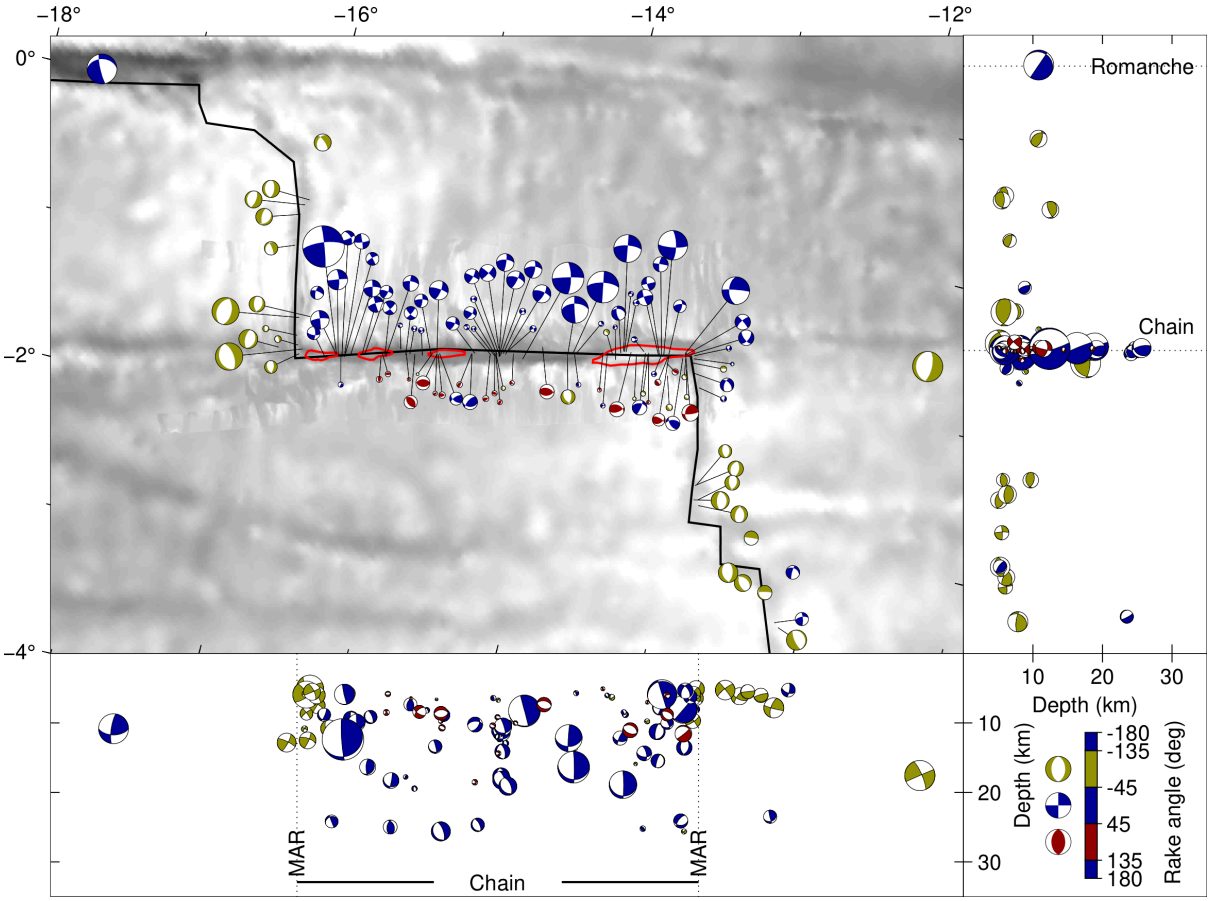

Fig. 5: Map including all focal mechanisms (shown as MT inversion results in Fig. 4). The mechanisms are placed apart from the OTF for better visibility. The shading is based on their dominant mechanism according to rake angle. Red lines indicate mapped transpressive flower-structures on the CTF (Harmon et al., 2018). See Figure 1 for further details. See Supplementary Table S2 for focal mechanism details. See Supplementary Figure S5 for an example of a waveform fit.

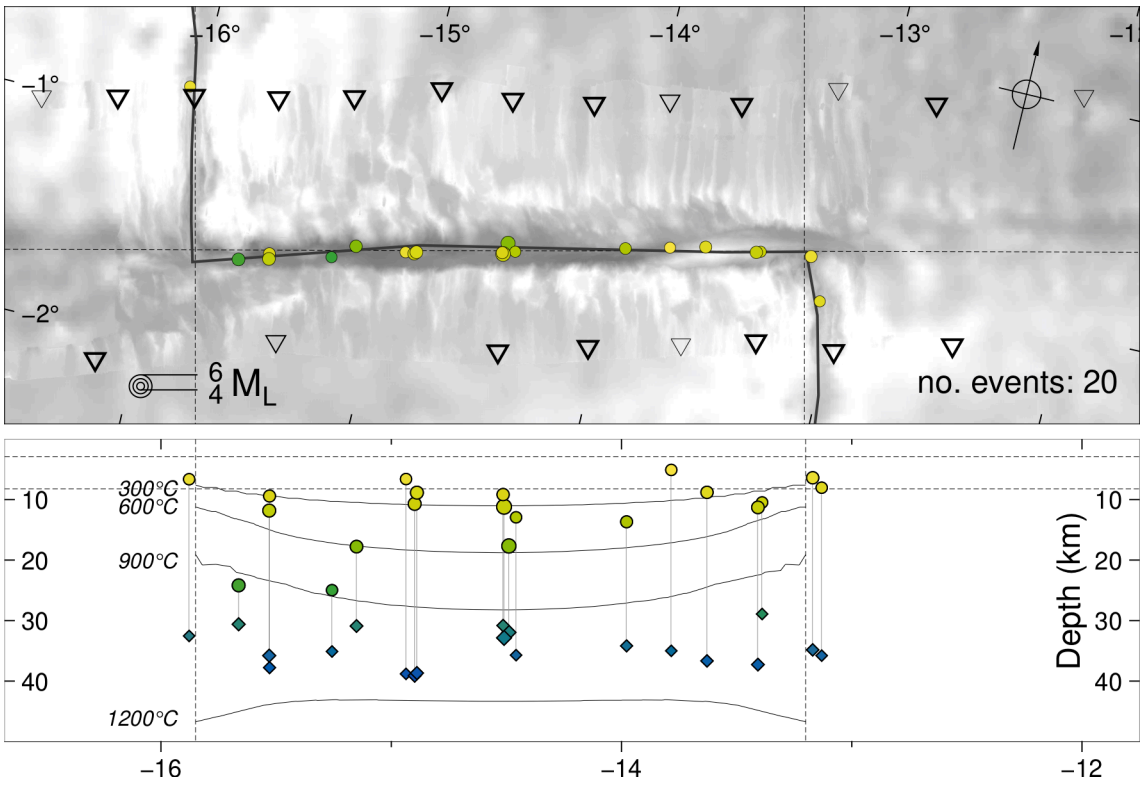

814

815 Fig. 6: Map showing all MT results that show a bimodal distribution with good shallow and

816 deep solutions, including shallow (circles) and deep (diamonds) in the cross section.